

Volumetric bounds on subsurface fluid substitution using 4D seismic time-shifts with an application at Sleipner, North Sea

P. Bergmann^{1,2} and R.A. Chadwick³

¹ SINTEF Petroleum Research, S.P. Andersens veg 15 A, 7031 Trondheim, Norway

² German Research Centre for Geosciences, Centre For Geological Storage, Telegrafenberg, 14467 Potsdam, Germany, bergmann@gfz-potsdam.de

³ British Geological Survey, Environmental Science Centre, Keyworth, Nottingham NG 12 5GG, United Kingdom, rach@bgs.ac.uk

Abstract

A method is presented for the volumetric estimation of subsurface fluid substitution based on the analysis of 4D seismic time-shifts. Since time-shifts cannot resolve for fluid saturation and layer thickness simultaneously without additional constraints, mass estimates are derived from the complete set of possible fluid saturations and layer thicknesses. The method considers velocity-saturation relationships that range from uniform fluid mixing to patchy fluid mixing. Based on a generalized velocity-saturation relationship that is parameterized by the degree of patchiness, explicit upper and lower fluid mass bounds are provided. We show that the inherent ambiguity between fluid saturation, fluid mixing and layer thickness has a severe impact on the convergence of these mass bounds. That is, fluid substitution scenarios with patchy fluid mixing and roughly linear velocity-saturation relationships allow for more accurate fluid quantification than scenarios associated with uniform mixing. Application of the method to two 4D seismic monitor data sets from Sleipner results in CO₂ mass bounds that are consistent with the true injected masses of CO₂. Moreover, a linear relationship between progressively developing 4D time-shifts and known injected CO₂ mass is observed, suggesting that the evolving patterns of fluid saturation and fluid mixing in the CO₂ plume have remained roughly constant with time.

Introduction

In recent years a variety of methods has been proposed to derive quantitative estimates on subsurface fluid substitution processes from time-lapse seismic data. For instance, Landrø (2001) introduced a method for discrimination of pressure and saturation changes from AVO data. Subsequently, Trani et al. (2011) refined this method by also including time-shifts in the analysis. For compacting reservoirs, time-shifts are used in order to monitor production

progress and related geomechanical issues (e.g. Guilbot and Smith, 2002; Landrø and Stammeijer, 2004).

Arts et al. (2004) and Chadwick et al. (2004, 2005) used time-shifts together with time-lapse reflection amplitudes to quantify the amount of CO₂ injected at the Sleipner site. In the same context, Ghaderi and Landrø (2009) introduced an analysis which exploits the angle-dependencies of amplitudes and time-shifts.

Through these studies it is evident that time-shift analysis is a mainstay in quantitative 4D seismic interpretation. Time-shifts provide complementary information compared with that provided by time-lapse reflection signals. Analysis of the latter, whilst potentially providing better vertical resolution, is often challenging due to prevalent interference of top and bottom reflections, inter-layer multiples, and various types of wave attenuation. In contrast, time-shifts provide a robust measure that integrates velocity changes over the depth intervals under investigation which can be particularly useful when dealing with fluid substitution in multiple thin, stacked layers.

However, the quality of a volumetric analysis that is solely based on time-shifts is inevitably limited due to the ambiguity of fluid layer thickness and fluid saturation. Because of this, it is common practice to include supplementary information in time-shift analyses. Apart from the examples mentioned above, such information could for instance be geophysical logs and depth dependent fluid properties (White, 2013), repeated logs and 4D reflection amplitudes (Ivanova et al., 2012), or analytical fluid migration solutions (Grude et al., 2014).

Another example is the combination of time-shifts and reflectivity tuning relationships, which allowed Chadwick et al. (2005) to partition high saturation CO₂ in thin reflective layers and much lower saturation CO₂ dispersed between them. This approach was used successfully for the first repeat (1999) dataset at Sleipner and a satisfactory match was obtained between imaged CO₂ distributions and known injected mass of CO₂. However, subsequent to the 1999 survey, the reflectivity of the deeper plume layers has declined progressively with time, due to a number of signal attenuation effects, and this approach is no longer viable.

As an alternative, we propose here to analyze time-shifts exclusively and without specifically resolving for layer thickness and saturation. Instead, we consider the complete set of possible layer thicknesses and saturation levels in order to deduce upper and lower bounds on the fluid mass, which are fully compliant with the inherent ambiguities. We will show that these bounds can provide useful estimates on actual fluid masses, particularly when the underlying velocity-saturation relationship is dictated by patchy fluid mixing. After introducing the method, an application to the Sleipner site will be used to assess its utility.

Method

The goal of this study is to use time-lapse seismic transit-time changes (time-shifts) to make volumetric estimates on subsurface fluid substitution processes. That is, obtaining lower and upper bounds for the mass of a fluid that is, while intruding into a subsurface formation, replacing an initially present fluid. In the following, the initial fluid will be referred to as fluid 1 and the intruding fluid will be referred to as fluid 2.

Figure 1 illustrates the two steps of the fluid substitution process under investigation. First, the case prior to fluid substitution, where a layer of thickness h_{\max} is entirely saturated with fluid 1. Secondly, the case after fluid substitution, where a portion of the same layer is saturated with a mixture of fluid 1 and fluid 2. The thickness of this layer portion will be denoted as h and its fluid 2 saturation as s_2 . Taking these two cases into consideration within

a repeated surface-seismic experiment, the two-way time-shift of a reflection event from beneath the fluid layer is (Chadwick et al., 2004):

$$\Delta t = 2h \left(\frac{1}{v(s_2)} - \frac{1}{v_1} \right), \quad (1)$$

where $v(s_2)$ is the seismic wave propagation velocity under the conditions of fluid 2 saturation and $v_1=v(s_2=0)$ the velocity at full fluid 1 saturation.

Hereafter, $v(s_2)$ will be referred to as velocity-saturation relationship.

The mass of fluid 2 per unit area is given by:

$$m = \phi \rho_2 h s_2, \quad (2)$$

where ϕ is the rock porosity and ρ_2 the density of fluid 2.

More precisely, m is the mass of fluid 2 which is contained in a vertical rock column defined by downward-projection of a unit area at the surface. Because of its dimensions (mass/length²), m will subsequently be denoted as mass per area. The total mass of fluid 2 integrated over a survey area is:

$$M = \sum_i a_i m_i, \quad (3)$$

where i is a consecutive surface location index and a_i the area associated with the surface locations (in practice, the CDP bin area).

Figure 2b illustrates the mass per area values computed for the full set of possible layer models (obtained by incrementing s_2 from 0 to 1 and h from 0 to h_{\max}) with $m_{\max}=\phi\rho_2h_{\max}$ being the maximum possible mass per area.

For the case of porous rock materials, the dependency of seismic velocity on pore fluid composition has widely been discussed, with the Gassmann model (Gassmann, 1951) and the patchy mixing model (e.g. Dvorkin and Nur, 1998) being the most prominent ones. The latter model is particularly relevant for heterogeneous reservoirs, as they tend to have patchy mixing due to “fingering” of pore-fluids, which can result from spatial variations in wettability, permeability or shaliness (Asveth, 2009). The two models in fact constitute upper and lower velocity bounds for the possible velocity-saturation relationships (Mavko and Mukerji, 1998) and relate to the relaxation of pressure perturbations induced by seismic wave passage. That is, assuming that patchy mixing can be described by geometric patches, which themselves are homogeneously saturated, there will be pressure exchange between nearby patches. On a larger scale, wave-induced pore-pressure differences should average to an equilibrated value. At a seismic wave frequency f , these pore pressure heterogeneities will equilibrate for scales smaller than the critical diffusion length (Mavko et al., 2003):

$$L_c \approx \sqrt{\frac{kK_{fl}}{f\eta}}, \quad (4)$$

with k denoting the rock permeability, K_{fl} the bulk modulus of the pore fluid, and η the fluid viscosity.

Uniform mixing exists if the patches are sufficiently small ($< L_c$), which leads to the fact that the pore-fluid mixture can be represented by a single effective fluid. Patchy saturation exists if the patches are larger than L_c , which leads to the case that spatial pressure fluctuations tend to persist during seismic wave passage.

In order to account for the variable characteristics of the velocity-saturation relations within these bounds, we introduce an arbitrary generalized velocity-saturation relationship:

$$v(s_2) = v_1 + \left(1 - \frac{p(1-s_2)}{p+s_2}\right) \Delta v \quad (5)$$

where $\Delta v = v_2 - v_1$ and $v_2 = v(s_2=1)$.

Figure 3 shows that the parameter p is specifying the degree of linearity in the velocity-saturation relationship. Since this is in turn conditioned by the type of fluid mixing, we will subsequently refer to p as the patchiness parameter.

Patchiness parameters larger than unity represent velocity-saturation relations associated with coarse-scale fluid mixing, whereas very small patchiness parameters approximate to Gassmann-type relations associated with uniform (homogeneous) fluid mixing. Inserting Equation 5 into Equation 1 yields the time-shift in dependence to the fluid 2 layer thickness and fluid 2 saturation:

$$\Delta t(h, s_2) = -\frac{2h(p+1)\Delta v s_2}{v_1(p+1)\Delta v s_2 + (p+s_2)v_1^2} \quad (6)$$

Using, as an example, a patchiness parameter of 0.07 and again the full set of possible layer models (as in Figure 2b), Figure 2c shows the time-shift as a function of s_2 and h . The maximum possible time-shift $\Delta t(h=h_{\max}, s_2=1)$ is denoted as Δt_{\max} .

Figure 2d shows the data points from Figures 2b and 2c rearranged into Δt and m axes, which is used because it is our aim to infer the mass per area m from an observed time-shift Δt . As an example, a vertical section through Figure 2d reveals those layer models, i.e. combinations of s_2 and h , which result in an equivalent time-shift.

When trying to estimate the mass per area solely from time-shifts, the distance between minimum and maximum m values with the same Δt defines the inherent ambiguity. This is conditioned by the fact that two different layers, e.g. one thin layer with high saturation and a second layer with larger thickness but lower saturation, can have different masses per area but may yield an identical time-shift. It is evident that the mass per area values that conform to a constant time-shift are constrained to certain mass ranges, which will subsequently be termed volumetric bounds. These bounds are illustrated in Figure 2d (black outline) and are given by (see Appendix A):

$$m_1 = -\frac{\rho_2 \phi v_1 (v_1 + \Delta v)}{2\Delta v} \Delta t \quad (7)$$

and:

$$m_2 = -\frac{\rho_2 \phi p v_1^2 h_{\max}}{(\Delta v(p+1) + v_1) v_1 \Delta t + 2(p+1)\Delta v h_{\max}} \Delta t \quad (8)$$

Generally, the m_1 -bound represents fully saturated fluid layers at variable thickness, e.g. cases where fluids are immiscible and residual saturation can be neglected. In contrast the

m_2 -bound represents those models which exhibit largest possible thicknesses at the lowest possible saturations (see s_{min} in Appendix A).

The dependence of the volumetric bounds with respect to the patchiness parameter is illustrated in Figure 4. Figure 4b points out the special case where the patchiness parameter takes the value:

$$p_{lin} = -\frac{v_1 + \Delta v}{\Delta v} \quad (9)$$

for which m_2 becomes equal to m_1 . More specifically, mass per area values can then exactly be determined using equation 7, implying that mass per area values scale linearly with time-shifts. Generally, this will rather be the case when the fluid mixing is dominantly patchy. For velocity-saturation relations with patchiness values lower than p_{lin} , m_1 constitutes the upper bound and m_2 the lower bound. Conversely, for $p > p_{lin}$, m_1 and m_2 constitute the lower and upper bounds, respectively.

Application at Sleipner

The Sleipner field is located in the Norwegian North Sea. Since 1996, CO₂ has been injected into a saline aquifer, the Utsira Sand, at approximately 1000 m depth. In order to monitor the spreading of the injected CO₂, 3D seismic data have repeatedly been acquired since 1994. The imaged data shows prominent brightening of nine reservoir level reflectors (Figure 5) and marked increases in interval transit-time across the Utsira Sand around the CO₂ plume (Figure 6). Based on these data a number of studies have been carried out, addressing the imaging and quantification of the injected CO₂. These studies comprise analyses of amplitude changes and time-shifts (Arts et al., 2004, 2008; Chadwick et al., 2004, 2005, 2009), their angle-dependencies (Ghaderi and Landrø, 2009; Buddensiek et al., 2010), underburden amplitude dimming (Boait et al., 2011), alternative processings using full-waveform inversion (Queißer and Singh, 2013a; 2013b; Romdhane et al., 2014), and evaluation of novel acquisition techniques (Furre and Eiken, 2014).

In order to exemplify the volumetric estimation method in the context of the Sleipner site, we begin with a synthetic example.

Synthetic example

Due to a lack of in-situ measurements and laboratory data, reported petrophysical models of the Utsira Sand have been deduced from rock physics modeling. For example, Arts et al. (2004) expect an initial p-wave velocity of 2050 m/s and a decrease by 600 m/s or more with CO₂ flooding. Queißer and Singh (2013a) proposed a similar model, which constrains the range of possible patchiness parameters by means of two end-member fluid mixing scenarios (a uniform mixing scenario and a patchy mixing scenario) (Figure 7). This range of possible mixing scenarios is conditioned by the spatial heterogeneity in lithology and fluid mobility in the Utsira Sand (Queißer and Singh, 2013a).

In preparation of the time-shift analysis, both end-member scenarios are fitted by means of the generalized velocity-saturation relationship in Equation 5. While obtaining $v_1=2050$ m/s, $\Delta v=-855$ m/s for both bounds, patchiness parameters of $p=0.03$ for the uniform mixing scenario and $p=0.7$ for the patchy mixing scenario are obtained, respectively. For the

purpose of our analysis these two patchiness parameters are assumed to encapsulate the range of possible velocity-saturation relations within the Utsira Sand.

Figure 8a shows the CO₂ layer model used in the synthetic study. In its left half, the model contains a CO₂ layer of constant saturation ($s_2=0.6$) and increasing thickness, representing a classical wedge model. At CDP station 7, the layer reaches a maximum thickness of 20 m. For larger CDP numbers, the layer thickness is kept constant and the saturation gradually decreased. Following Arts et al. (2004), the porosity is set to 0.37 and CO₂ density to 650 kg/m³.

Figures 8b and 8c show the velocity-saturation relationships together with the respective m_1 and m_2 functions. The synthetic seismograms are shown in Figures 8d and 8e. Beneath the CO₂ fluid layer, the model comprises a reflector which is used for determination of the time-shifts shown in Figures 8f and 8g. Gray patches in Figures 8h and 8i show the upper and lower mass bounds obtained from the time-shifts and give a comparison with the true values (blue line).

Because being relatively close to $p_{lin} \approx 1.4$ (which is obtained from Equation 8 with $v_1=2050$ m/s and $\Delta v=-855$), it can be seen that the patchy mixing scenario ($p=0.7$) is yielding fairly confined bounds. At CDP station 6 for instance, the mass per area is inferred to be in the range 2.52 ± 0.21 tons/m² (true value 2.41 tons/m²). For the uniform mixing scenario ($p=0.03$), a range of 2.35 ± 1.53 tons/m² is obtained which is displaying rather poorly confined bounds. This is a result of the very low patchiness parameter, which leads to a saturation sensitivity that is virtually confined to the first few percent of CO₂ saturation.

Real data application

Chadwick et al. (2004) pointed out the saturation-related uncertainty in calculating CO₂ masses from time-shifts and presented models for the Sleipner dataset from 1999 based on maximum and minimum saturation end-members. Here we present the more systematic time-shift analysis introduced above, focusing on the 1994 baseline seismic dataset and two repeat vintages from 2001 and 2006.

To this end, the velocity-saturation relationships from the aforementioned synthetic study will be used and we take the same values for porosity and CO₂ saturation. Following Arts et al. (2004), the reservoir thickness h_{max} is set to 200 m, since now the entire thickness of the Utsira Sand is under investigation. With this reservoir thickness, we obtain mass per area functions as shown in Figure 9.

Taking the 1994 and 2001 datasets first, with a true CO₂ injected mass of 4.26 Mtons in 2001, measured increases in interval transit-time (time-shifts) across the Utsira Sand range up to about 40 ms (Figure 6a). These dwarf the very small residual time-shifts at the top of the Utsira Sand, which are due to time-lapse acquisition mismatches and show an average of -0.15 ms. There is also a small 0.11 ms average transit-time increase measured within the reservoir but outside of the saturation footprint of the CO₂ plume (Figure 6c). This is interpreted as a systematic effect associated with pressure change in the reservoir (a detailed discussion on this is provided by Chadwick et al., 2012). In order to isolate the time-shifts due solely to fluid saturation changes, this pressure-related offset was subtracted from the gross measured transit-time changes prior to mapping out the maximum and minimum mass per area values over the survey area (Figures 10a and 10b).

It should be noted that negative time-shifts yield negative mass per area values (indicated by dotted line portions in Figure 9). Given that small positive errors will most likely balance out the negative ones, we include the entire set of time-shifts from Figure 6a in the total mass

computation, rather than restricting the analysis to an arbitrarily thresholded CO₂ plume footprint.

Finally, the total masses M_1 and M_2 are obtained from the summation over the mass per area values, using Equation 3 and a CMP bin area of 12.5×12.5 m² (Figure 10). Figure 10c provides a summary on the total mass values within the bounds set by the end-member mixing scenarios. For the uniform mixing scenario ($p=0.03$), a total CO₂ mass of $M=0.3\text{--}5.3$ Mtons is obtained. For the patchy mixing scenario ($p=0.7$), a total CO₂ mass of $M=4.0\text{--}5.3$ Mtons is obtained.

The 2006 dataset (Figure 6b), corresponding to a true injected CO₂ mass of 8.4 Mtons, shows maximum changes in transit-time in excess of 50 ms, albeit with greater uncertainty than for the 2001 data due to increasing signal attenuation beneath the plume. Performing the same analysis gives inferred total masses of $M=0.7\text{--}10.9$ Mtons for the uniform mixing scenario and $M=8.2\text{--}10.9$ Mtons for the patchy mixing scenario (Figure 11).

Discussion

Up to now, the time-shift analysis was presented in the context of fluid injection. However, it is also adaptable to cases of fluid extraction through the following modifications: Fluid 2 is to be redefined as fluid that is inflowing after fluid 1 has been extracted. Furthermore, the reservoir thickness h_{\max} is to be redefined as the depth distance between the top of the reservoir and the pre-extraction fluid contact (Figure 12).

It is also interesting to note that velocity-saturation relationships lying in the intermediate range between the uniform and patchy mixing bounds, are similar to velocity-saturation relations obtained from Brie's model (Brie et al., 1995; Figure 7). In fact, this is because the patchiness parameter p in equation 5 is playing a similar role to the exponential parameter e in Brie's model. Apart from this, it should be noted that equation 5 has a limitation in representing Gassmann-type velocity-saturation relations, in that it cannot produce the (density-related) velocity minimum, which is typically occurring in the range of low to moderate saturations (in particular for rocks with high permeability and porosity).

Following Boait et al. (2012) in presuming that the CO₂ at Sleipner is tending towards uniform mixing within the highly saturated layers and patchy mixing elsewhere, the notable divergence of M_1 and M_2 observed for the uniform scenario is an expression of the ambiguity between CO₂ saturation and CO₂ layer thickness. In accordance with the previous observations, it is seen that time-shift analysis is most suitable for reservoirs which are characterized by patchy mixing.

Error sensitivity of the mass estimate

In order to investigate the error sensitivity of the volumetric results from Sleipner with respect to inaccuracies in the input parameters, we use as an example the total CO₂ masses obtained for the 2006 dataset in the patchy mixing scenario ($p=0.7$, $M_1=7.5$ Mtons, $M_2=10.0$ Mtons, Figure 11c). Error sensitivities are assessed by computing relative changes of M_1 and M_2 after successively perturbing the input parameters by $\pm 10\%$ (Figure 13). Although it is from a practical point of view obvious that a 10% perturbation in reservoir thickness cannot rigorously be compared to, for example, a 10% perturbation in porosity, the following conclusions can be made:

(a) Most significant error sensitivities arise for the velocity parameters in the petrophysical

model. In other words, inaccuracies in v_1 and Δv , which can be significant for lithologically heterogeneous reservoirs, are likely the most important error contributors to the total mass.

(b) The patchiness parameter has no influence on M_1 and, at least for the investigated patchy mixing case, only a moderate impact on M_2 .

(c) Inaccuracies in porosity and the CO_2 density scale linearly into M_1 and M_2 .

(d) Inaccuracies in time-shifts scale linearly into M_1 and nearly linearly into M_2 .

(e) Since the reservoir thickness h plays no role for M_1 , and ranks lowest among the parameter sensitivities for M_2 , it may be considered as the most tolerable error contributor to the total mass.

Are fluid mixing characteristics at Sleipner varying over time?

The above analysis underlines the sensitivity of time-shifts with respect to both the degree of CO_2 saturation and the type of fluid mixing. Considering also the ambiguity between CO_2 saturation and CO_2 layer thickness, it is obvious that unique solutions for the CO_2 distribution in the reservoir cannot be obtained from time-shifts alone. Beyond the assessment of volumetric bounds, however, time-shifts can be used to provide constraints on the fluid mixing characteristics in the reservoir.

The Sleipner 4D seismic data indicate that reflectivity change and velocity time-shifts evolve in conjunction with each other. With time, however, progressively increasing reflectivity in the shallower part of the plume is observed to be in marked contrast to progressively decreasing reflectivity in the deeper part (Figure 5).

Although, the reasons behind this are not yet fully understood, it is clear that a number of wave propagation effects are relevant in this regard. Most importantly, the temporally increasing amount of CO_2 contained within the plume will lead to increased layer reflectivity, intra-layer scattering, and intrinsic attenuation, all of which tend to cause reflection dimming in the deeper plume layers. On the other hand, once a region has been swept by CO_2 , its effective permeability to CO_2 flow will increase and the possibility of enhanced buoyancy-driven migration through the thin intra-reservoir layer seals leading to real reduction of CO_2 saturations in the deeper reservoir cannot be ruled out.

The 4D time-shifts cast a light on this uncertainty. Time-shifts associated with the plume (Figure 6) can be integrated across the area of the plume footprint, providing the spatially integrated time-shift value (with units of m^2s). Interestingly, this value shows an approximately linear relationship with the known injected mass of CO_2 (Figure 14).

Given the high sensitivity of time-shifts with respect to both fluid saturations and to fluid mixing, the observed linearity indicates that the principal characteristics of the velocity-saturation in the CO_2 -swept regions have remained rather constant throughout the twelve years investigated. Dwindling or disappearance of CO_2 layers in the deeper reservoir would cause a change in the vertical distribution of the CO_2 saturation in the plume which would likely give rise to a progressive non-linearity in the time-shift response.

This is an important monitoring observation, because it suggests that the deeper CO_2 layers, although being progressively less well imaged with time, are still present. In other words, the

sustained correlation between measured time-shifts and injected CO₂ mass indicates that the brine-CO₂ mixing characteristics in the Utsira Sand are rather stable over time.

Conclusions

We have presented a method for volumetric estimation of subsurface fluid substitution that is based on the analysis of 4D seismic time-shifts. The method comprises three steps: (1) Fitting of a generalized velocity-saturation relation to available petrophysical data; (2) Calculation of lower and upper bounds which set time-shifts in relation to fluid masses; (3) Conversion of observed time-shift maps to fluid mass maps.

The lower and upper bounds provided by the method take into account the limitations arising from the ambiguity of fluid saturation, layer thickness and fluid mixing. In other words, because the analysis is based on time-shifts alone, the resulting masses are assessed within uncertainty bounds, which consider the complete set of possible fluid distributions and layer thicknesses. It was found that scenarios where subsurface fluid mixing is patchy can be more accurately quantitatively bounded than scenarios where fluid mixing is uniform. In this respect it is noted that reservoirs which are markedly heterogeneous, with strong layering, might be expected to be associated with patchy fluid mixing patterns to a greater degree than more homogenous reservoirs.

The method was demonstrated using a simple synthetic model and real time-lapse data from the Sleipner storage site. Calculated volumetric bounds were found to be consistent with the known amounts of CO₂ injected at Sleipner. While relatively tight volumetric bounds were obtained for the patchy fluid mixing scenario, only the upper bound was found useful for the uniform fluid mixing scenario.

The study emphasizes the sensitivity of time-shifts with respect to fluid saturation and fluid mixing behavior, and we have found, over the twelve-year period under investigation at Sleipner, a consistent linear correlation between measured time-shifts and injected CO₂ mass. This indicates that the distribution of CO₂ saturations within the plume and its fluid mixing characteristics have remained temporally rather constant.

Acknowledgements

This publication was produced with partial support from the COMPLETE project, which is funded by the Federal Ministry of Education and Research, VGS, RWE, Vattenfall, Statoil, OMV, and the Norwegian CLIMIT programme.

Additional support has come from the BIGCCS Centre, performed under the Norwegian research programme Centres for Environment-friendly Energy Research (FME). The authors acknowledge the following partners for their contributions: ConocoPhillips, Gassco, Shell, Statoil, TOTAL, GDF SUEZ and the Research Council of Norway (193816/S60). Andy Chadwick publishes with the permission of the Executive Director, British Geological Survey (NERC).

We thank the SACS, CO₂ReMoVe and the license partners of PL046 (Statoil Petroleum AS, ExxonMobil Exploration & Production Norway AS and Total E&P Norge AS) for data release. We thank Anne-Kari Furre, Robert Benson, and three anonymous reviewers for helpful comments on the manuscript.

Appendix A - Derivation of volumetric bounds

Non-zero time-shifts cannot yield arbitrarily small mass per area values (Figure 2d). In turn, time-shifts cannot be caused by arbitrarily low fluid 2 saturation. That is, even in cases where fluid 2 is present within the entire reservoir thickness ($h=h_{max}$), a minimum fluid 2 saturation

$$s_{min} = -\frac{pv_1^2}{\Delta tv_1 (\Delta v (p+1) + v_1) + 2\Delta v h_{max} (p+1)} \Delta t \quad (A-1)$$

is required to yield a given time-shift. The fluid 2 saturation s_2 will therefore always lie between s_{min} and 1.

The level curve $h(s_2)$ with $\Delta t(h, s_2)=const.$ (displayed by the contours in Figure 2c) can be obtained from substituting Equation 5 into Equation 1 and solving for h . Substitution of $h(s_2)$ into Equation 2 then yields:

$$m(s_2) = -\frac{\phi \rho_2 v_1 (\Delta v s_2 (p+1) + v_1 (p+s_2))}{2\Delta v (p+1)} \Delta t. \quad (A-2)$$

Because Equation 11 is monotonous in s_2 , $m(s_{min})$ and $m(1)$ will be extreme values, which correspond to the sought volumetric bounds.

Let $s_2=1$ define the first bound, m_1 . This bound can be deduced from setting $s_2=1$ in Equation 11, resulting in Equation 7. Alternatively, m_1 can be obtained by means of $m_{max}=\phi \rho_2 h_{max}$ and Δt_{max} (see Equation 6). Since $s_2=1$ represents a fluid 2 layer at full saturation, the time-shift will be proportional to the mass per area. Because the maximum possible mass per area m_{max} is yielding the maximum possible time-shift Δt_{max} , Equation 7 can also be read as:

$$m_1 = \frac{m_{max}}{\Delta t_{max}} \Delta t. \quad (A-3)$$

Let the second bound, m_2 , be given by $s_2=s_{min}$. This bound, is deduced from substitution of Equation 10 into Equation 11, resulting in Equation 8.

In the limit of an infinite patchiness parameter, i.e. a linear velocity-saturation relation (Figure A-1, green line), the m_2 bound reads:

$$\lim_{p \rightarrow \infty} m_2 = \frac{h_{max} \phi \rho_2 v_1^2 \Delta t}{\Delta v (2h_{max} + v_1 \Delta t)}. \quad (A-4)$$

References

- Arts, R., O. Eiken, A. Chadwick, P. Zweigel, L. Van Der Meer, and B. Zinszner, 2004, Monitoring of CO₂ injected at Sleipner using time-lapse seismic data: *Energy*, 29, 1383-1392.
- Arts, R., A. Chadwick, O. Eiken, S. Thibeau, and S. Nooner, 2008, Ten years' experience of monitoring CO₂ injection in the Utsira Sand at Sleipner, offshore Norway: *First break*, 26, 65-72.
- Asveth, P., 2009, Exploration Rock Physics – The Link between Geological Processes and Geophysical Observables, *in* Bjørlykke, K., ed., *Petroleum Geology*: Springer, 403-426.
- Boait, F., N. White, A. Chadwick, D. Noy, and M. Bickle, 2011, Layer spreading and dimming within the CO₂ at the Sleipner field in the North Sea: *Energy Procedia*, 4, 3254-3261.
- Brie, A., F. Pampuri, A. Marsala, and O. Meazza, 1995, Shear sonic interpretation in gas-bearing sands: 70th SPE Annual Technical Conference and Exhibition, paper SPE 30595.
- Buddensiek, M., S. Sturton, and M. Dillen, 2010, AVO analysis of thin layers - application to CO₂ storage at Sleipner: 72nd Conference and Exhibition, EAGE, Extended Abstracts, P303.
- Chadwick, R.A., R. Arts, O. Eiken, G.A. Kirby, E. Lindeberg, and P. Zweigel, 2004, 4D seismic imaging of an injected CO₂ bubble at the Sleipner Field, central North Sea *in* R.J. Davies, J.A. Cartwright, S.A. Stewart, M. Lappin and J.R. Underhill, eds, *3-D Seismic Technology: Application to the Exploration of Sedimentary Basins*: Geological Society, London, Memoir 29, 305-314.
- Chadwick, R., R. Arts, and O. Eiken, 2005, 4D seismic quantification of a growing CO₂ plume at Sleipner, North Sea: Geological Society, London, *Petroleum Geology Conference series*, 6, 1385-1399.
- Chadwick, R., D. Noy, R. Arts, and O. Eiken, 2009, Latest time-lapse seismic data from Sleipner yield new insights into CO₂ plume development: *Energy Procedia*, 1, 2103-2110.
- Chadwick, R., G. Williams, J. Williams, and D. Noy, 2012, Measuring pressure performance of a large saline aquifer during industrial-scale CO₂ injection: The Utsira sand, Norwegian North Sea: *International Journal of Greenhouse Gas Control*, 10, 374-388.
- Dvorkin, J., and A. Nur, 1998, Acoustic signatures of patchy saturation: *International Journal of Solids and Structures*, 35, 4803-4810.
- Furre, A.-K., and O. Eiken, 2014, Dual sensor streamer technology used in Sleipner CO₂ injection monitoring: *Geophysical Prospecting*, 62, 1075-1088.
- Gassmann, F., 1951, Über die Elastizität poröser Medien: *Vierteljahresschrift der Naturforschenden Gesellschaft Zürich*, 96, 1-24.
- Ghaderi, A., and M. Landrø, 2009, Estimation of thickness and velocity changes of injected carbon dioxide layers from prestack time-lapse seismic data: *Geophysics*, 74, no. 2, O17-O28.
- Guilbot, J., and B. Smith, 2002, 4-d constrained depth conversion for reservoir compaction estimation: Application to Ekofisk field: *The Leading Edge*, 21, 302-308.

Grude, S., M. Landrø, J.C. White, and O. Torsæter, 2014, CO₂ saturation and thickness predictions in the Tubåen Fm., Snøhvit field, from analytical solution and time-lapse seismic data: *International Journal of Greenhouse Gas Control*, 29, 248-255.

Ivanova, A., A. Kashubin, N. Juhojuntti, J. Kummerow, J. Henniges, C. Juhlin, S. Lüth, and M. Ivandic, 2012, Monitoring and volumetric estimation of injected CO₂ using 4D seismic, petrophysical data, core measurements and well logging: A case study at Ketzin, Germany: *Geophysical Prospecting*, 60, 957-973.

Landrø, M., 2001, Discrimination between pressure and fluid saturation changes from time-lapse seismic data: *Geophysics*, 66, no. 3, 836-844.

Landrø, M., and J. Stammeijer, 2004, Quantitative estimation of compaction and velocity changes using 4D impedance and travelttime changes: *Geophysics*, 69, no. 4, 949-957.
Mavko, G., and T. Mukerji, 1998, Bounds on low-frequency seismic velocities in partially saturated rocks: *Geophysics*, 63, no. 3, 918-924.

Mavko, G., T. Mukerji, and J. Dvorkin, 2003, *The Rock Physics Handbook: Tools for seismic analysis of porous media*, Cambridge University Press.

Queisser, M., and S. C. Singh, 2013a, Full waveform inversion in the time lapse mode applied to CO₂ storage at Sleipner: *Geophysical Prospecting*, 61, 537-555.

Queisser, M., and S. C. Singh, 2013b, Localizing CO₂ at Sleipner - Seismic images versus p-wave velocities from waveform inversion: *Geophysics*, 78, no. 3, B131-B146.

Romdhane, A., E. Querendez, and C. Ravaut, 2014, CO₂ thin-layer detection at the Sleipner field with full waveform inversion: Application to synthetic and real data: *Energy Procedia*, 51, 281-288.

Trani, M., R. Arts, O. Leeuwenburgh, and J. Brouwer, 2011, Estimation of changes in saturation and pressure from 4D seismic AVO and time-shift analysis: *Geophysics*, 76, no. 2, C1-C17.

White, D., 2013, Toward quantitative CO₂ storage estimates from time-lapse 3D seismic travel times: An example from the IEA-GHG Weyburn-Midale CO₂ monitoring and storage project: *International Journal of Greenhouse Gas Control*, 16, Supplement 1, S95 - S102.

Figures

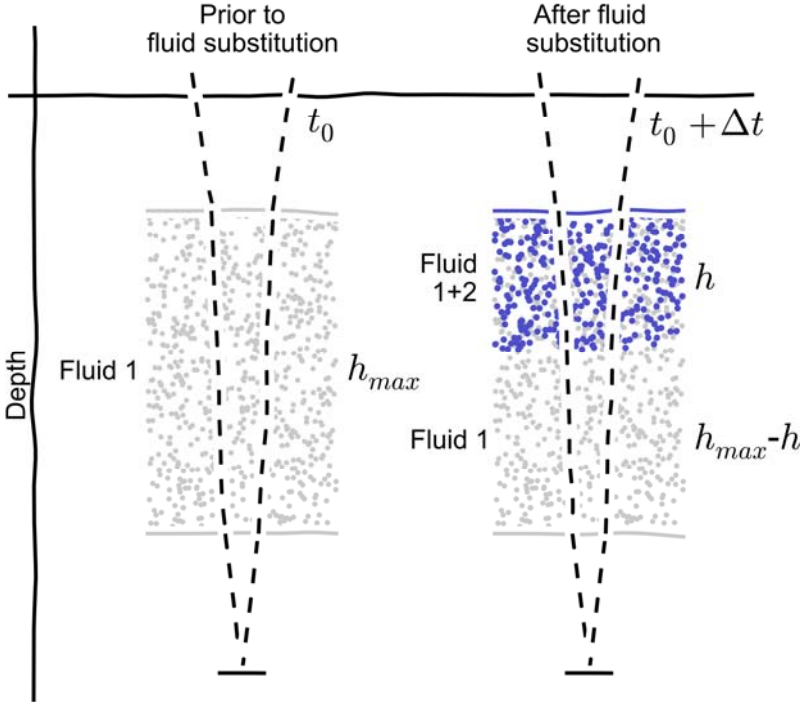


Figure 1: Sketch of the fluid substitution process taking place within a reservoir layer of the thickness h_{max} . A time-lapse seismic experiment is carried out comprising measurements in the stages before and after fluid substitution. The dashed lines represent a small-offset ray path with reflection below the reservoir. Two-way-time of the ray in the baseline stage denotes as t_0 . Time-shift after fluid substitution denotes as Δt .

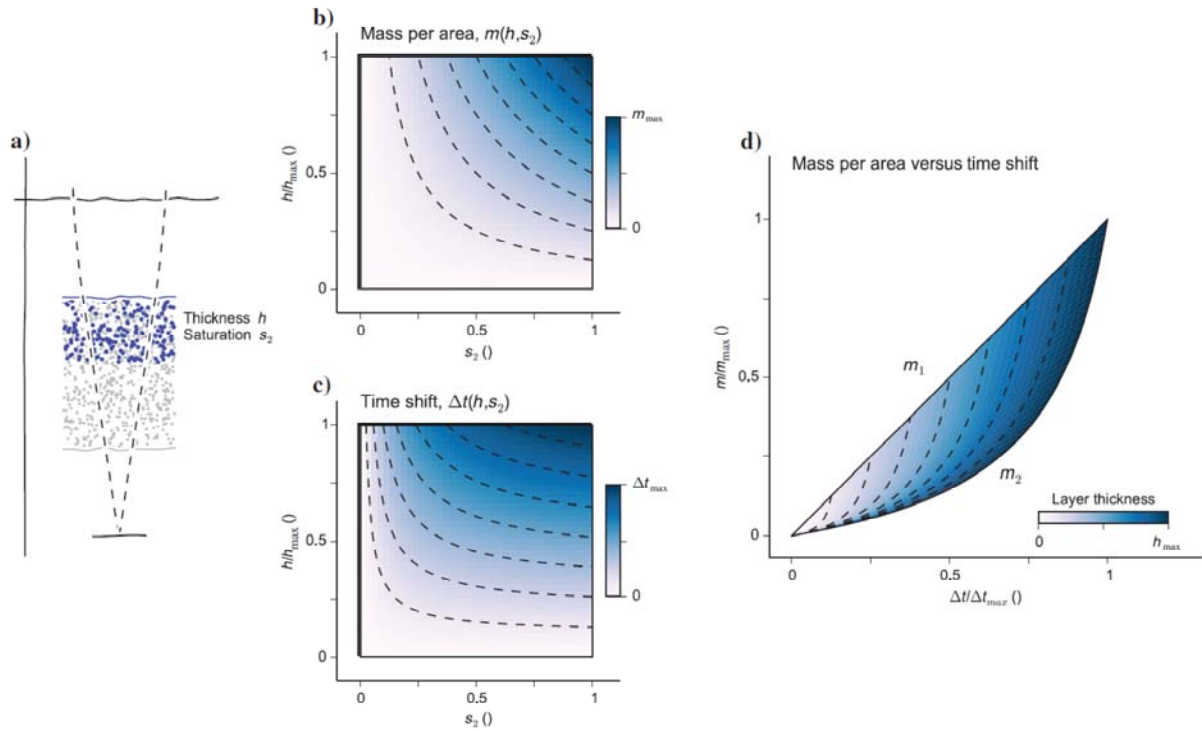


Figure 2: a) Fluid layer model as in Figure 1 being fully specified by its layer thickness h and fluid 2 saturation s_2 . b) Mass per area, m , in dependence of h and s_2 . c) Time-shift, Δt , in dependence of h and s_2 (computed with Equation 6 using $p=0.07$, $v_1=2.1$ km/s, $\Delta v=-1.3$ km/s, $h_{max}=20$ m, $\Phi=0.2$, and $\rho_2=300$ kg/m³). d) Rearrangement of the models shown in b) and c) into Δt and m axes.

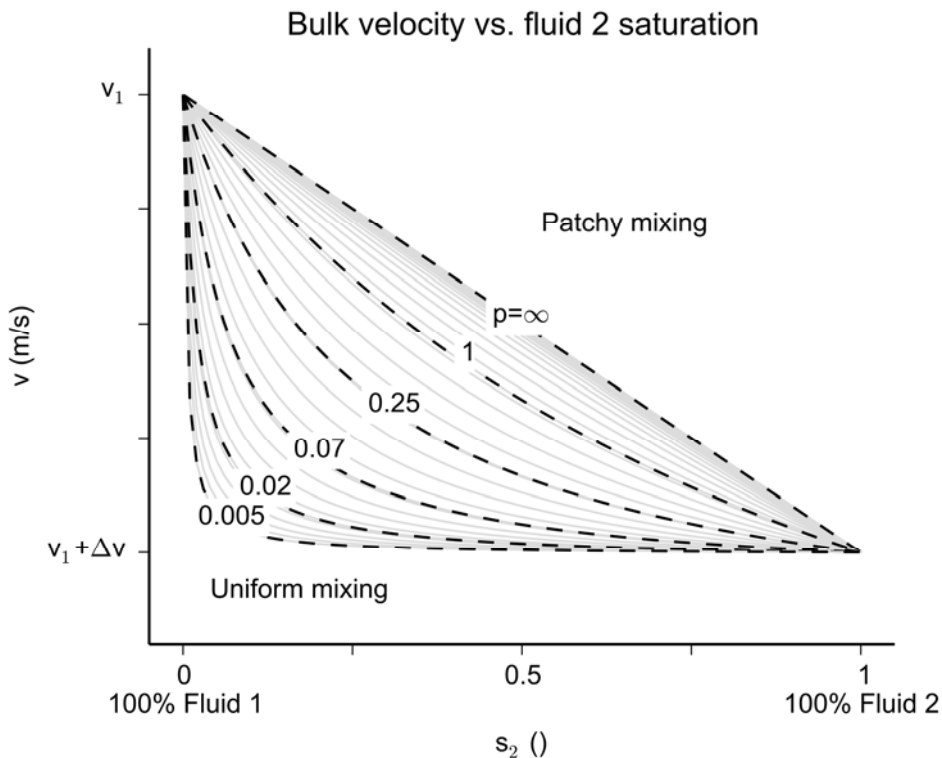


Figure 3: Set of velocity-saturation relations computed from Equation 5 using a variable patchiness parameter (marked graphs).

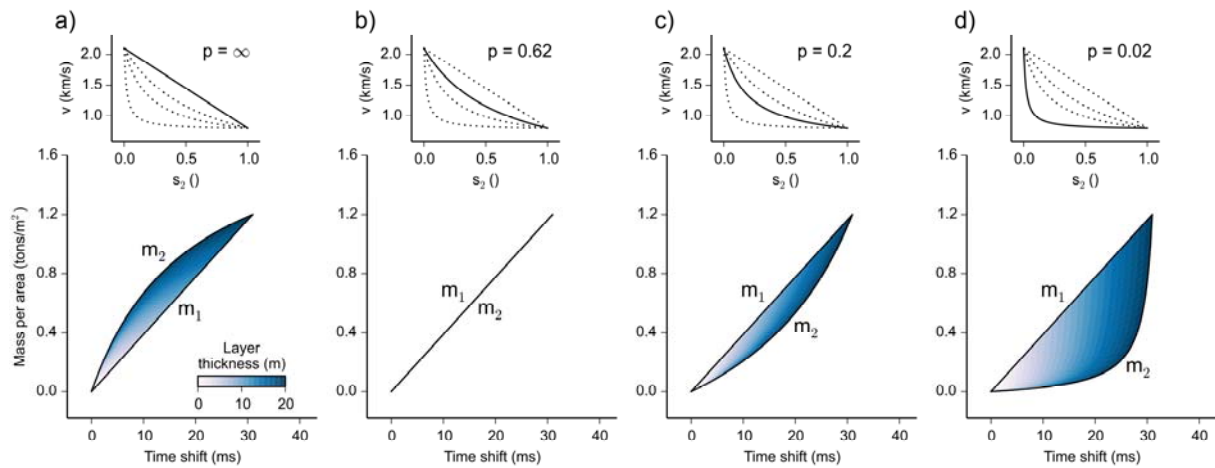


Figure 4: Volumetric bounds, m_1 and m_2 , illustrated for different patchiness parameters. Other input parameters used in this figure are $v_1=2.1$ km/s, $\Delta v=-1.3$ km/s, $h_{\max}=20$ m, $\Phi=0.2$, and $\rho_2=300$ kg/m³.

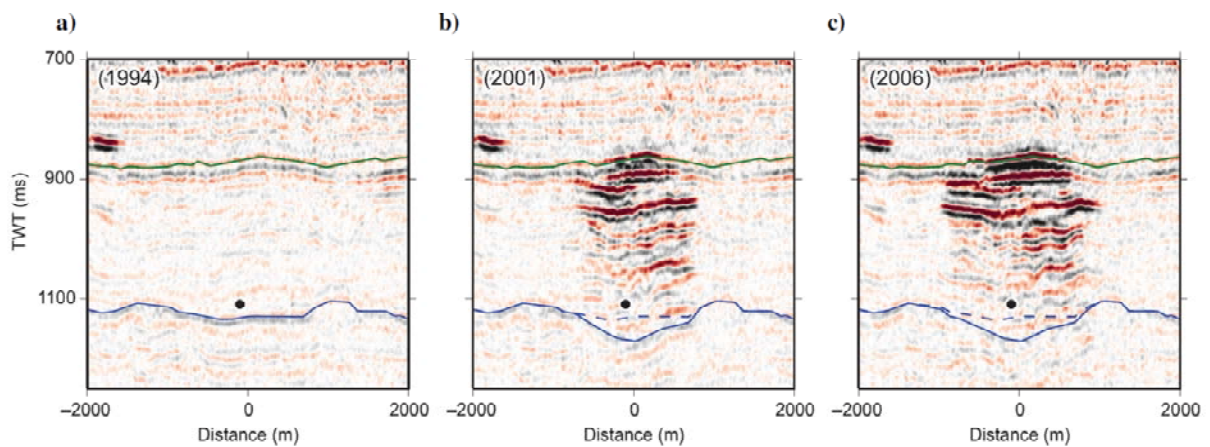


Figure 5: Stacked inline section through the injection area for the 1994 (pre-injection), 2001, and 2006 data. Green and blue lines show top and bottom horizon picks of the Utsira Sand, respectively. Black marker denotes projected injection point.

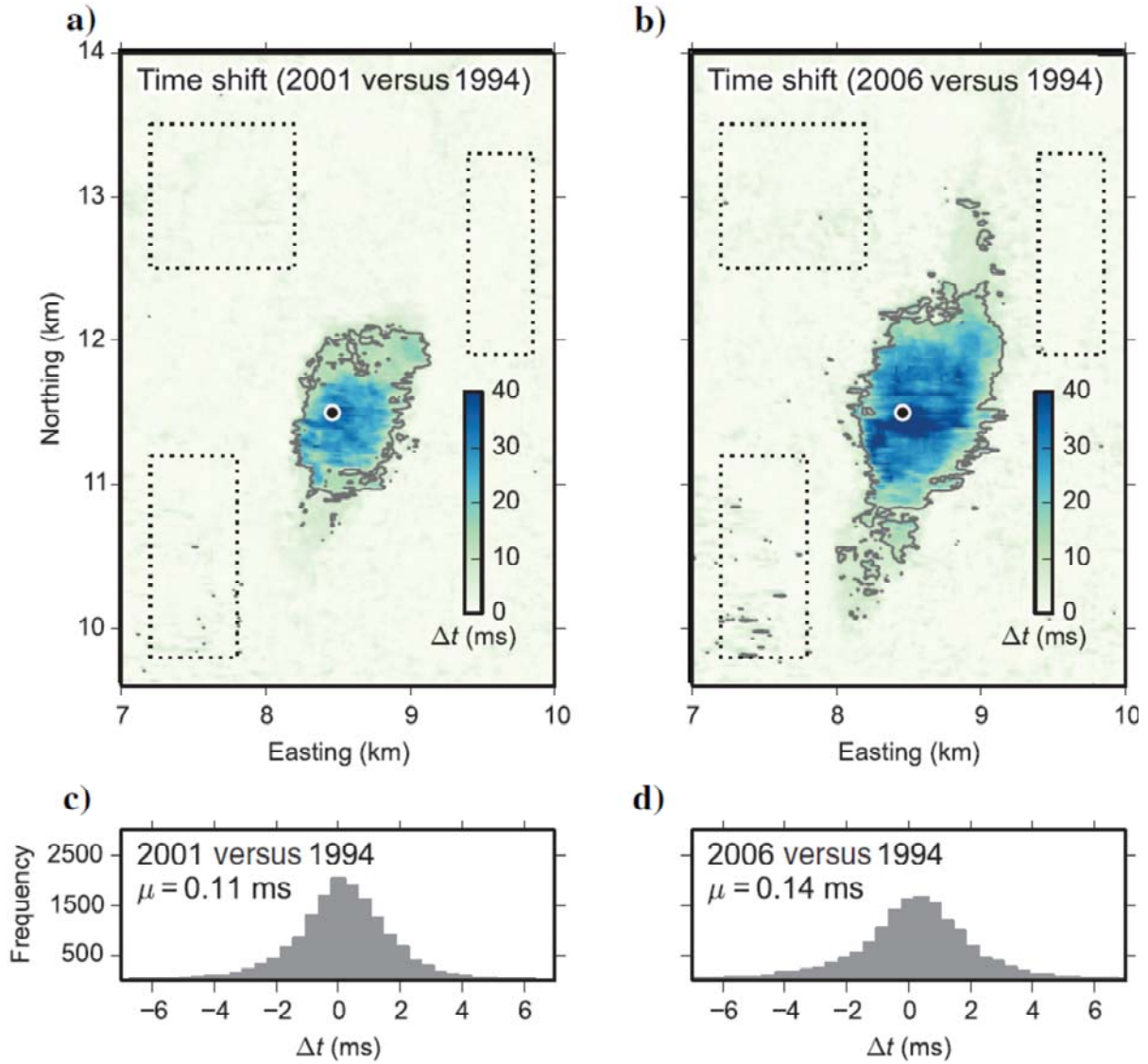


Figure 6: Plan view of the increases in seismic transit-time through the Utsira Sand reported by Chadwick et al. (2012) for the 2001 and 2006 data. Black marker denotes injection point. For visual orientation, contour line marking $\Delta t=10$ ms has been added. c-d) Transit-time change histograms obtained from representative data subsets outside the injection-related time-lapse anomaly. Corresponding subset areas mark by dotted outlines, respectively.

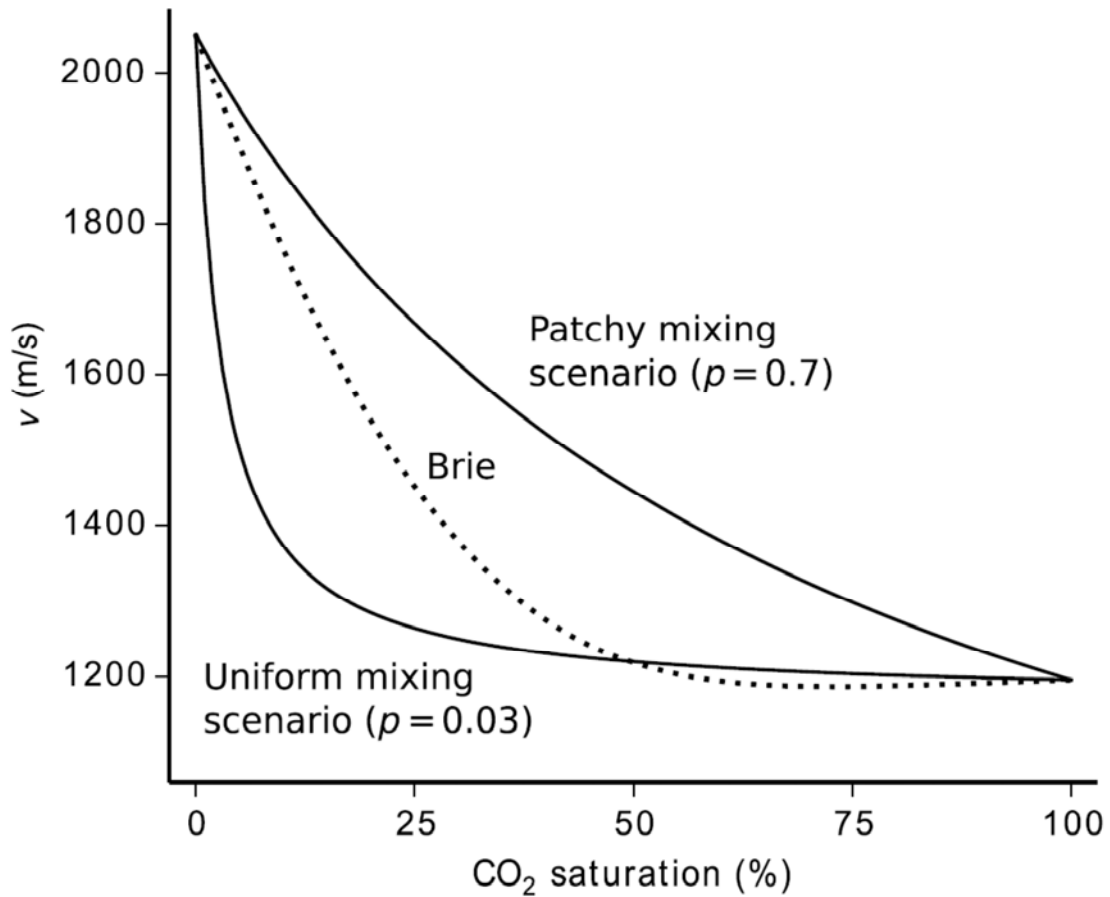


Figure 7: Petrophysical velocity-saturation model of the Utsira sand after Queier and Singh (2013a). The model comprises upper and lower bounds on the velocity-saturation relation, which are fitted by Equation 5 using $v_1=2050$ m/s, $\Delta v=-855$ m/s and the patchiness parameters marked at the graphs. The dashed curve shows an intermediate velocity-saturation relationship deduced by Queier and Singh (2013a) on the basis of Brie's model (Brie et al., 1995).

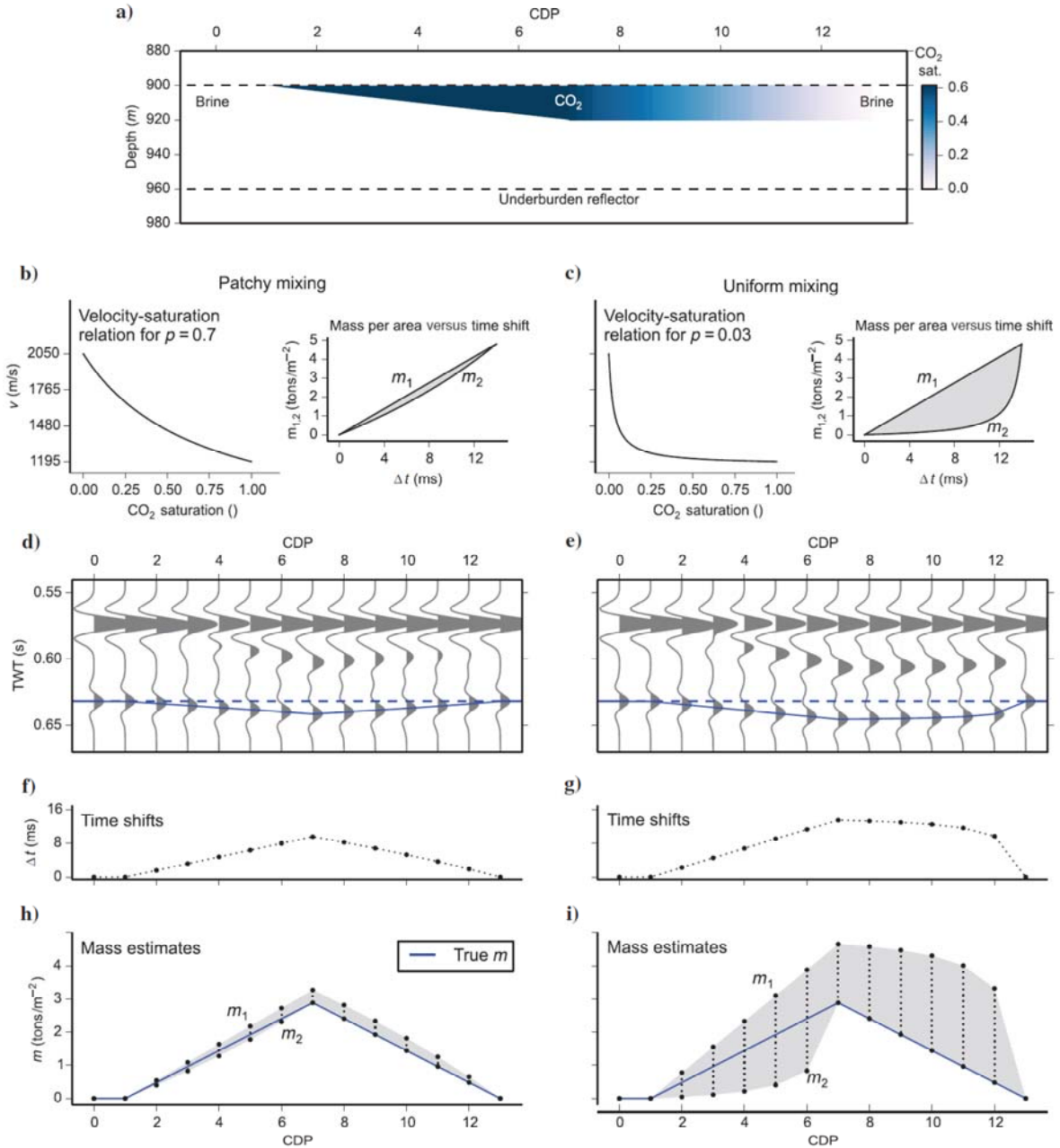


Figure 8: Mass estimation example for a simple wedge model. a) A fluid 2 layer with spatially variable thickness and saturation constituting the model after fluid substitution. b) and c): Velocity-saturation relationships for different patchiness parameters and their resulting mass per area bounds m_1 and m_2 (shown by inlays). d) and e): Synthetic seismograms. f) and g): Resulting time-shifts. h) and i): Mass per area bounds deduced from time-shifts and comparison with true mass per area values.

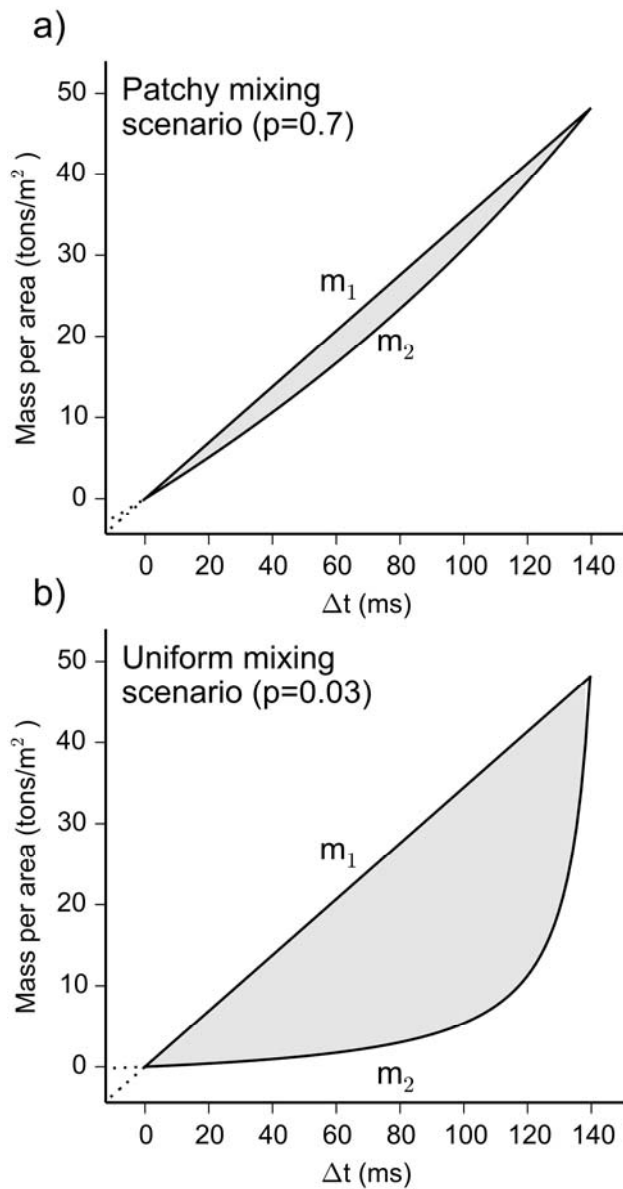


Figure 9: a) Mass per area bounds m_1 and m_2 for the patchy mixing scenario and b) for the uniform mixing scenario.

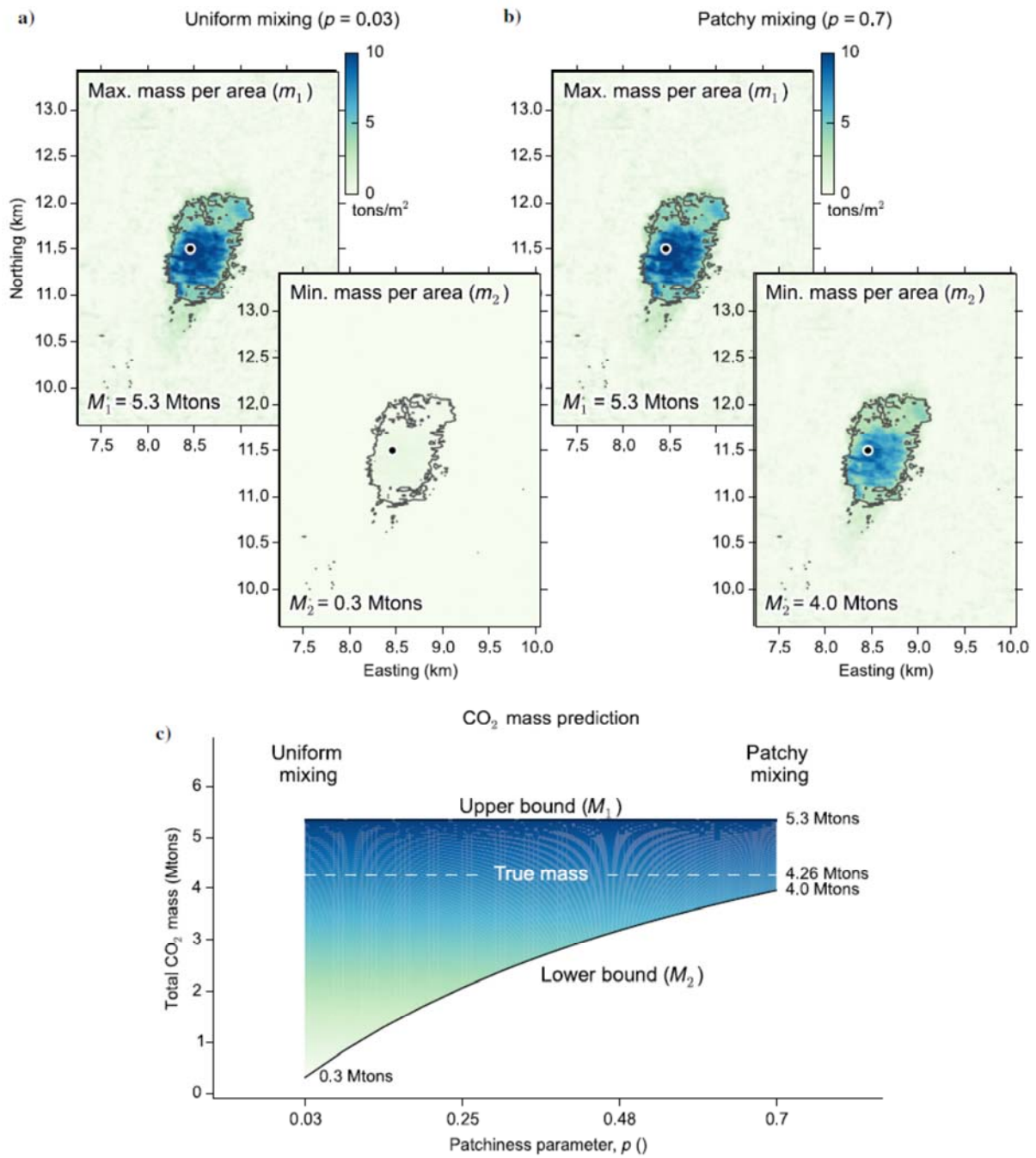


Figure 10: Mass inference for the 2001 dataset. a) Minimum and maximum mass per area maps for the lower (uniform mixing) velocity-saturation bound ($\rho=0.03$). M_1 and M_2 refer to the total mass values deduced from using m_1 and m_2 as input parameters in Equation 3. b) Minimum and maximum mass per area maps for the upper (patchy mixing) velocity-saturation bound ($\rho=0.7$). For visual orientation, contour line marking $\Delta t=10$ ms has been added. c) Inferred total mass bounds plotted against patchiness parameter.

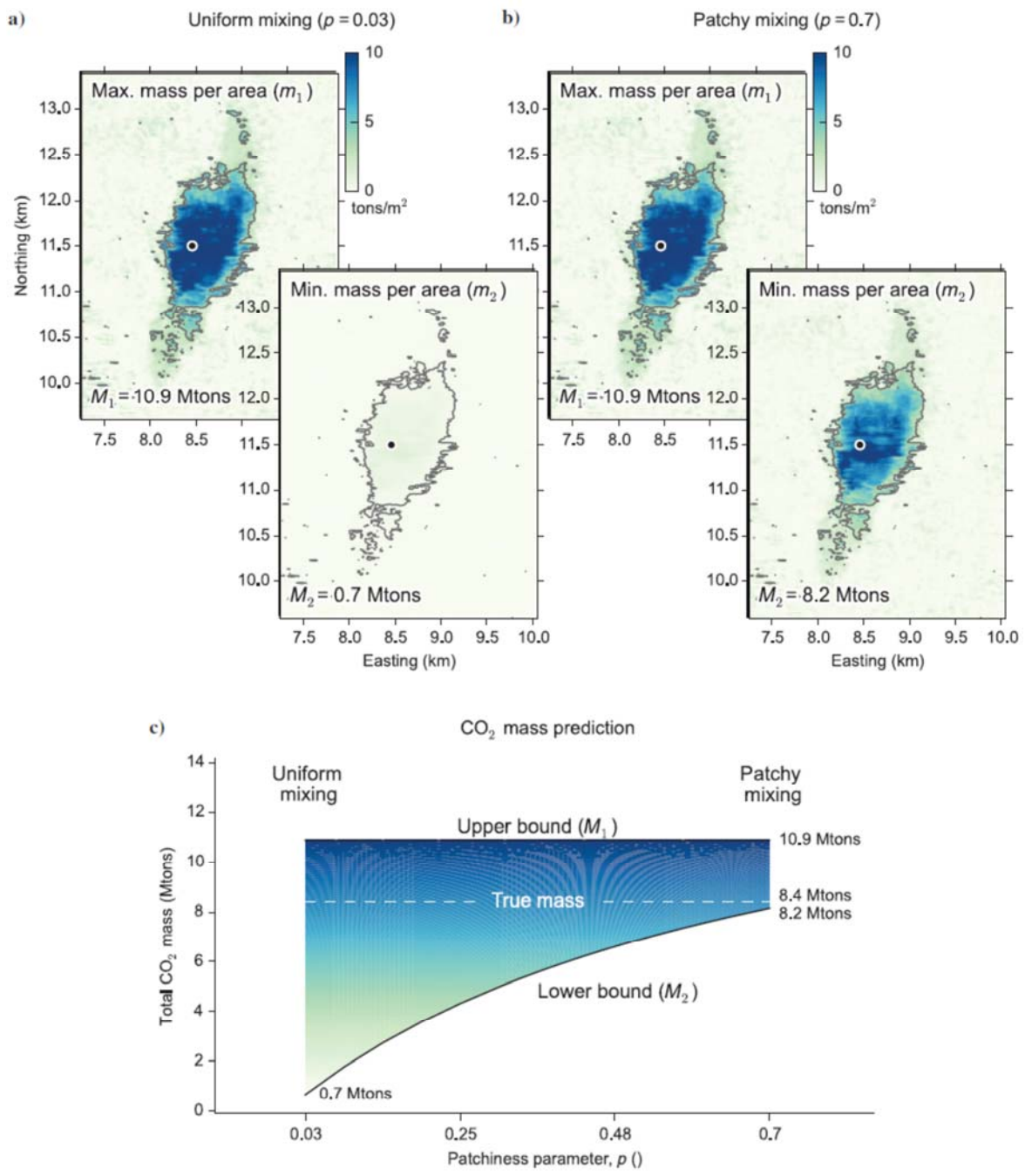


Figure 11: Mass inference for the 2006 dataset. a) Minimum and maximum mass per area maps for the lower (uniform mixing) velocity-saturation bound ($p=0.03$). b) Minimum and maximum mass per area maps for the upper (patchy mixing) velocity-saturation bound ($p=0.7$). For visual orientation, contour line marking $\Delta t=10$ ms has been added. c) Inferred total mass bounds plotted against patchiness parameter.

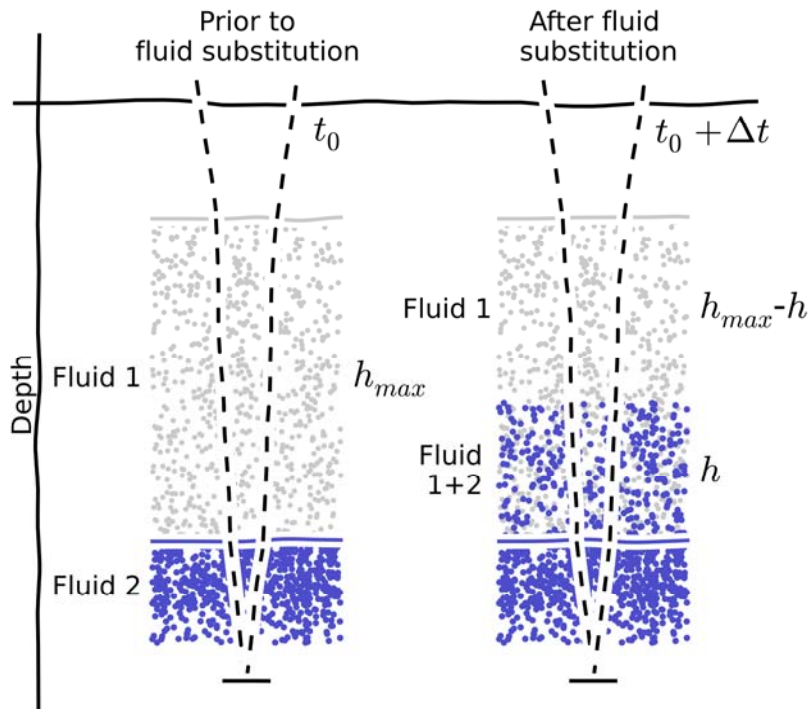


Figure 12: Sketch of a fluid substitution process illustrating the production case.

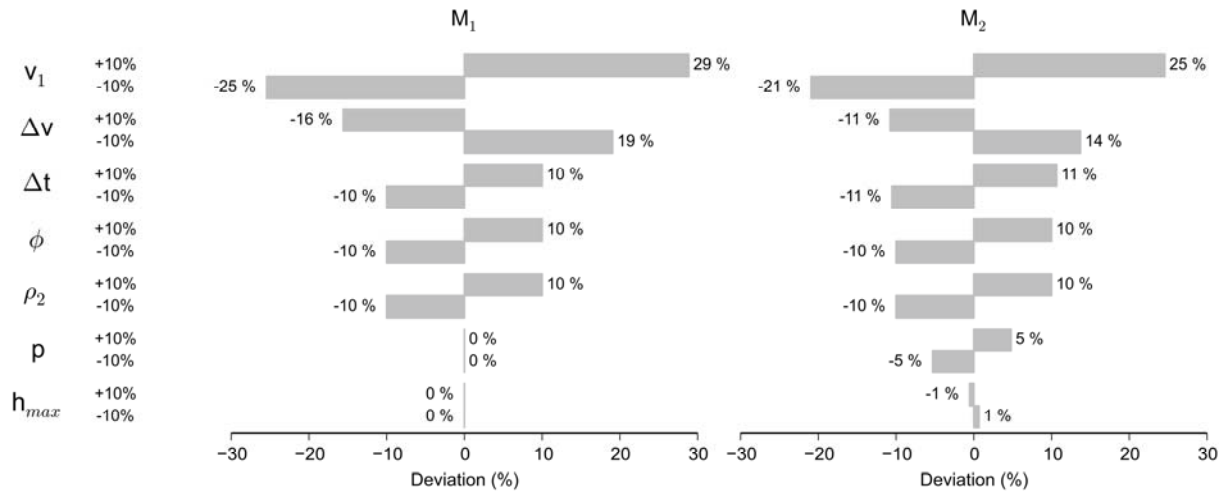


Figure 13: Sensivities of the total mass bounds with respect to $\pm 10\%$ perturbation in the input parameters. Sensivities have been computed on the basis of the M_1 and M_2 values inferred from the 2006 data for the patchy mixing scenario (Figure 11c).

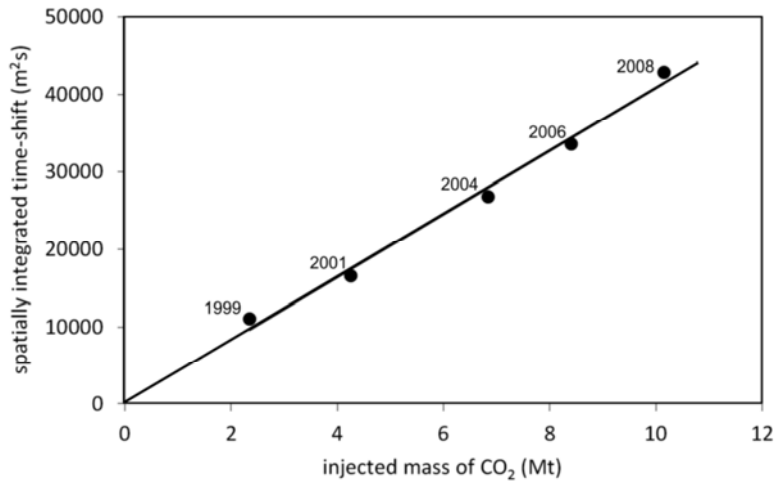


Figure 14: Spatially integrated time-shift measured at base Utsira Sand beneath the Sleipner CO₂ plume, plotted against measured injected amount.

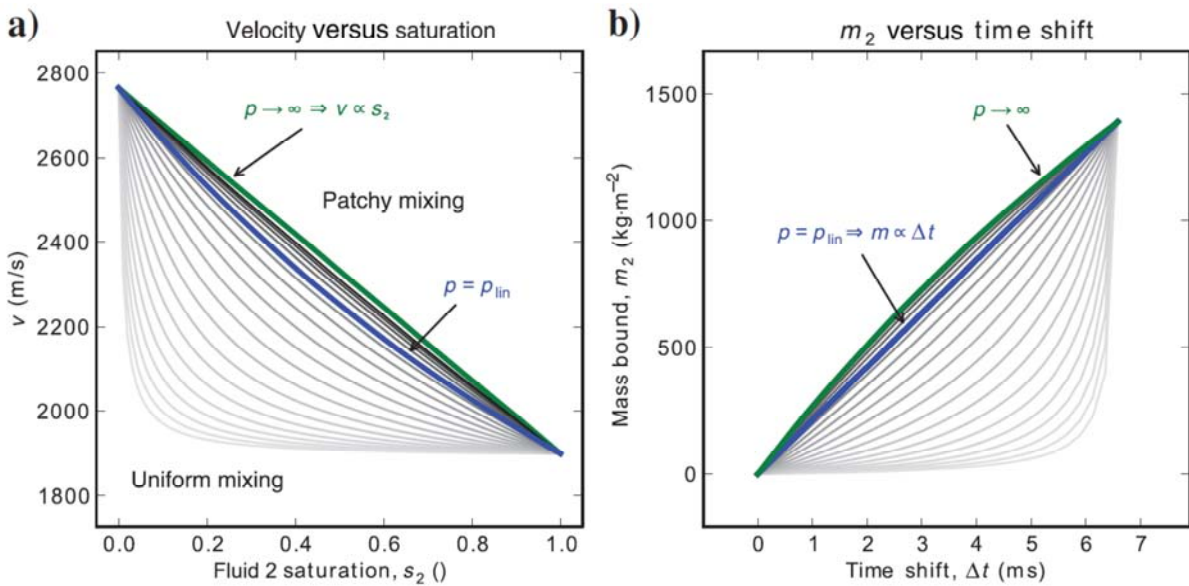


Figure A-1: Impact of the patchiness on the velocity-saturation relationship (a) and the m_2 -bound (b). Shades from light to dark gray indicate increasing patchiness parameters. Input parameters used in this figure are $v_1 = 2765$ m/s, $\Delta v = -865$ m/s, $h_{\max} = 20$ m, $\Phi = 0.3$, and $\rho_2 = 231.59$ kg/m³.